Microstructural Characterization of the Transition in SS316L and IN625 Bimetallic Fabricated Using Hybrid Additive Manufacturing

Christopher J.Bettencourt[1] and Nadia Kouraytem[1*]

[1]Mechanical and Aerospace Engineering Department, Utah State University, Logan, Utah 84322-4130.
[*]Corresponding author: nadia.kouraytem@usu.edu.

Abstract

Nearly all energy technologies utilize heat exchangers and recuperators within the power cycle. To further improve the cost-effectiveness of recuperators, costly high temperature Inconel 625 superalloy was substituted with a more affordable Stainless Steel 316L to be used at the low-temperature side of the heat exchanger. Bimetallic samples for analysis and examination were fabricated by combining Laser Powder-bed Fusion and Directed Energy Deposition. Two transition strategies for joining to the laser powder-bed fusion steel were explored, namely, a direct transition and an intermediate layer of 50% nickel powder mixed with 50% steel powder through Directed Energy Deposition. The microstructure and chemical composition of the multi-material structures were compared to the single alloy counterparts. Iron rich regions within the 50/50 transition zone suggest elemental segregation during the deposition of the 50/50 mixed zone. Vickers hardness values measured using micro-indentation are presented across both types of transitions and show a relative lower value in the 50/50 mixed zone.

Keywords: Functionally Graded Materials, Hybrid Additive Manufacturing, Microstructure, Steel, Nickel-based Superalloy

1 Introduction

Energy consumption is projected to increase as much as 15% while the United States has the goal to reach net zero Greenhouse Gas Emissions by 2050 [1–3]. This requires renewable energy sources to replace fossil fuel sources while simultaneously ramping production to meet ever-growing energy demand. Specifically, Concentrated Solar Power (CSP) has recently gained attention due to its potential for producing clean energy at a reasonable cost [4, 5].

One of the challenges holding back CSP from being more widely implemented is the cost of fabricating recuperators (heat exchangers). High-temperature recuperators alone account for 25-30% of the overall turbo-generator cost in a power system [6]. To enable higher cost effectiveness, substituting the high-temperature material with a low cost material has been explored. McDonald estimated a cost savings of 60% if SS347 was substituted with IN625 in a counterflow recuperator used for microturbine applications [7]. McDonald proposed the substitution of IN625 by SS347 using an automated spiral foil wrapping fabrication method.

Combining alloys is referred to as multi-material, bimetallics, or Functionally Graded Materials (FGM). FGMs have become popular over the last 20 years where yearly publications on the topic have tripled since the year 2000 [8]. Over the past decade, manufacturing FGMs has been shifting from traditional methods such as, vapor deposition, thermal spray, and powder metallurgy, to Additive Manufacturing (AM) due to the design freedom, reduced manufacturing steps, lower cost, and better production cycles [9–11].

AM is a suite of manufacturing processes in which materials are fabricated in a layer-by-layer method to yield a three-dimensional part. Of interest to metal fabrication, Laser Powder Bed Fusion (LPBF) is a common process of AM in which the metal powder is swept onto the build plate one layer at a time then particles are selectively fused using a high-powered laser, the build plate is lowered and the cycle is repeated. Directed Energy Deposition (DED) on the other hand is an AM process that is gaining popularity especially in large scale manufacturing and repair. DED deposits powder or wire feedstock concentrically with a high powered laser which simultaneously melts the material as it is deposited. DED results in lower resolution parts and larger feature capabilities when compared to LPBF. DED machines are sometimes equiped with several hoppers that enable depositing of multi-materials, in contrast, LPBF requires changing powder feedstock or making expensive upgrades to equipment to make multi-material fabrication possible.

To help enable future multi-material heat exchangers to be manufactured by AM technologies, more knowledge must be disseminated about its potential for increasing affordability. Recuperators are being built by AM to enable compact design, consolidation of component assemblies, and ability to manufacture multi-material components [12–14]. Six other case studies are reviewed by Kaur and Singh [15]. Very few multi-material heat exchangers have been fabricated by AM techniques [16, 17].

Two widely used metallic alloys are Stainless Steel 316L (SS316L) and Inconel 625 (IN625). SS316L provides high performance in mechanical properties and increased corrosion resistance at a low cost when compared to other similar materials [18]. IN625 on the other hand is a high-temperature alloy that is nonmagnetic, corrosion - and oxidation-resistant and is used for its high strength and toughness [19]. The combination of these alloys can provide material cost savings when compared to using IN625 as a single material.

The joining of the two dissimilar metals has been covered in detail from various research groups. Zhang et al. [20] tested the properties of graded IN625 with SS316L compared to single alloy counterparts processed by DED. The results showed sharp microstructural variations for the direct transition sample and gradual variations for the graded layer samples. The yield strength of the graded samples approached that of pure IN625 and ultimate strength was similar to pure SS316L. Su et al. [21] demonstrated the effect of different mixing ratios throughout the gradation of Laser Metal Deposited SS316L and IN718 multi-material. The conclusion was a transition of 10% composition change every 10 layers for the intermediate layers between alloys provided the highest tensile properties and elongation, while decreasing the intermediate zone mixing to 5% produced thermal cracking. Hinojos et al. [22] deposited IN718 onto a SS316L substrate and SS316L onto a IN718 substrate using powder-bed Electron Beam Melting. Joints were characterized and it was concluded that the electron beam melting method was superior at producing a bimetallic than traditionally welded joints. Chen et al. [23] studied the effect of build parameters on properties during deposition of IN718 tracks joined onto a SS316H substrate through LPBF. The authors concluded that chemical inhomogeneity may benefit the mechanical properties by providing interlocking between the two materials. Singh et al. [24] produced a SS316L and IN718 bimetallic with an intermediate layer between the pure alloys using LPBF and found a parameter set that produced defect free bimetallics. The tensile strength approached that of SS316L. The microstructure showed columnar grains and equiaxed grains within the transition region. Shah et al. [25] performed a parametric study of SS316L with IN718 manufactured via DED. Phases were identified, tensile, wear, and hardness properties measured while exploring the effect of varying the laser power parameter. The authors concluded that the processing parameters of DED (i.e., laser power and powder mass flow rate) were inversely proportional to the tensile strength of the functional part.

The objective of this research is the investigation of the microstructure and microhardness of a combination of LPBF SS316L and DED IN625 to manufacture a bimetallic. This combination of techniques can leverage the advantages of each AM technique (small features in LPBF and fast deposition in DED) and can be used as a reference for the repair of a LPBF part by DED using a dissimilar metal. In this research, a direct transition specimen and a 50/50 transition specimen were assessed to enable future research and application of bimetallic and functionally graded heat exchangers.

2 Methodology

In this investigation, single and bimaterial samples were manufactured using AM processes for examination of the microstructures. The SS316L and IN625 materials were manufactured using LPBF and DED, respectively, and the pure single alloys were examined as reference materials. Bimaterial samples were manufactured by depositing DED IN625 onto LPBF SS316L. Two transition strategies were investigated, namely a direct transition in which no mixing of powders occurred and a 50/50 mixing strategy in which the two alloy powders were mixed during the DED process for two layers (600 µm) before the transition to pure DED IN625. See appendix **Figures 7,8** for critical characteristics of both alloys from literature values.

2.1 Fabrication

2.1.1 Laser Powder Bed Fusion

The SS316L powder used was made by gas atomization by Praxair. The Additive Industries MetalFAB1 was used to produce the SS316L single alloy as well as the SS316L section of the bi-metallic specimens. Argon was used as inert gas in the build chamber. The system was equipped with four SPI Red Power (500-Watt, 1,070 wavelength) lasers with full field coverage that allow it to produce several parts at once or work on larger parts with all four lasers capable of scanning a single part simultaneously. A layer thickness of 50 µm and a chess scanning strategy was used. Recommended optimal processing parameters were used by Addman Engineering to fabricate the SS316L and are detailed in **Table 1**. The LPBF parts were stress-relieved through a ramp up to 450°C and held at that temperature for 4 hours, then

Table 1 Process Parameters for LPBF SS316L and DED IN625 Alloys

			LPBF SS316L			
	Hatch Spacing (µm)	Hatch Speed (mm/s)	Hatch Power (W)	Contour Speed (mm/s)	Contour Power (W)	
	100	850	220	850	100	
			DED IN625			
Power	Feed Rate (mm/min)	Flow Rate (g/min)	Spot Dia. (mm)	Shield Gas (l/min)	Carrier Gas (l/min)	Hatch Space Overlap (%)
MPSC[1]	Contour: 600 Infill: 800	18.75	2.5	14	7	35

[1]Melt Pool Size Control (MPSC) is the in-situ closed-loop feedback cycle used by Formalloy to vary the laser power to maintain the set melt pool size, which is detected by an optical camera.

Table 2 Composition of prominent elements of Praxair SS316 powder (weight %)

Fe	Cr	Ni	Mo	Si	Mn
Balance	16.87	12.16	2.39	0.5	0.46

furnace cooled to 200°C and air cooled to room temperature and removed from the substrate through wire electrical-discharge machining. For the elemental composition of the SS316L powders, see **Table 2**.

2.1.2 Directed Energy Deposition

During DED, metal powder is deposited onto the build via a blown gas coaxial with a high-powered laser that melts the newly deposited powder onto the previously deposited layers. IN625 was deposited directly onto the LPBF SS316L specimen for the direct transition. A two layer intermediate mixture (300 µm each, hence a total of 600 µm) of 50% SS316L with 50% IN625 was deposited onto the LPBF SS316L for the 50/50 transition before deposition of the 100% IN625 alloy. The powders were blended during deposition from their respective hoppers. The IN625 powder was manufactured by Praxair Surface Technologies via vacuum induction argon gas atomization.

Table 3 Composition of prominent elements Praxair NI-328-17 powder (weight %)

Ni	Cr	Mo	Fe	Nb	Co
Balance	21.38	9.09	4.00	3.72	0.10

The apparent density per ASTM B212 was 4.16 (g/cm^3) The elemental composition is shown in **Table 3**. The FormAlloy L5 machine was used to fabricate the IN625. Argon gas was used as a shielding and carrier gas. The machines were equipped with a 1 kW fiber laser. FormAlloy employs in-situ build data monitoring for analysis and real-time closed-loop control. The build parameters for the IN625 are shown in **Table 1** and are set point values that may have varied over the build to control melt pool geometry. The test coupons were machined to thickness before experimentation.

2.2 Electron Backscatter Diffraction

Scanning Electron Microscopy (SEM) imaging was captured for the single material and transition zones of the bimetallic specimens. Samples were ground and polished on a Buehler grinder-polisher machine, vibratory polished, and cleaned with an ultrasonic bath for several hours. Images were captured using an FEI Quanta FEG 650 SEM equipped with Electron Backscatter Disfraction (EBSD) capabilities using a NordlysMax Detector and Energy Dispersive Spectroscopy (EDS) capabilities using an Oxford X-Max Detector. The accelerating voltage was 30 kV, with a spot size of 4.5 µm, and a dwell time of 40 µs. For the EBSD analysis, the step size was 3 µm with forward scatter enabled. AZtec software was used to post-process the EBSD data and generate the inverse pole figure (IPF) maps, grain texture pole figures, and grain size distribution data. For the calculation of the average grain size, the maximum Feret diameter was used as a measure.

2.3 Micro-hardness

The Vickers micro-hardness property of the single and bimaterials was tested using a witness sample with both transitions implemented into one part and tested at FormAlloy. The sample was fabricated by depositing DED IN625 onto a LPBF SS316L block using a direct transition on the bottom of the SS316L block and and a 50/50 transition in which 50% of SS316L powder is mixed with 50% IN625 powder is deposited on the top of the SS316L block. The surface was polished and tested using an ALPHA-MHT-1000Z microhardness tester produced by Pace Technologies. Three repetition for each single material and transition zone were performed and averaged. More information about the part geometry and results are presented in Section 3.2.

3 Results and Discussions

3.1 Single Alloys

The IPF map, grain size distribution, and pole figures of the LPBF SS316L are shown in **Figure 1**. The sample exhibits a relatively fine microstructure with grains that align with the build direction in the LPBF process, see Figure 1. The average grain diameter measured using maximum Feret diameter is 35.6 µm. The standard deviation is 20.7 µm with the median being 28.5 µm. The distribution of grain diameters illustrates the high frequency of smaller sized grains demonstrating a right skew of larger grains with a maximum of 177 µm. The average area of the grains is 360 μm^2 and average aspect ratio of 2.28. The maximum misorientation angle is 20°. High concentration of crystallographic orientation in the inverse pole figure is observed in the [101] crystallographic direction for the Y inverse pole figure. These results are in agreement with the general trend of grain orientations in LPBF SS316L [26–28].

The DED IN625, on the other hand, exhibits larger grains when compared with SS316L, as shown in Figure 2 (note that both EBSD IPF maps were captured at the same resolution for ease of interpretation). The average grain diameter in DED IN625 is of 80.24 µm with a standard deviation of 86.96 µm and a median of 48.8 µm. The texture is shown in the inverse pole figures of **Figure 2**. The grains are textured again in the [101] crystallographic direction of the Y inverse pole figure as well as in the [111] crystallographic direction in the X IPF texture map, which correspond to the build direction. These results are also in agreement with the general trend of the anisotropy in AM Nickel-based alloys [29–32].

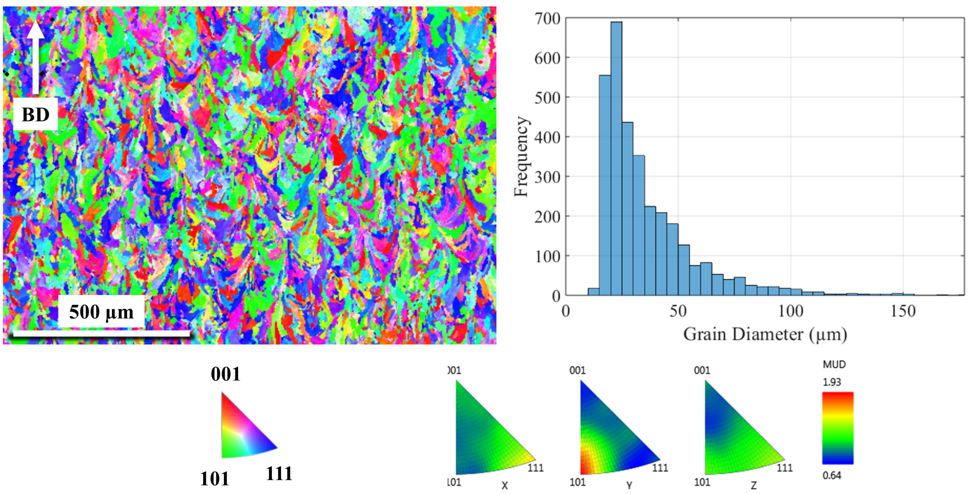

Fig. 1 Single alloy LPBF SS316L IPFZ maps, grain size distribution, and pole figures. The build direction is identified with an arrow on the IPF map.

3.2 Dual Materials

The microstructural characterization for the two transition strategies of the dual materials are compared side by side in **Figure 3**. The band contrast BSE and IPF maps are compared side by side for the direct transition on the left and the 50/50 transition on the right. The transition zones in each transition strategy are identified using dashed lines on the band contrast images and further labeled. The band contrast

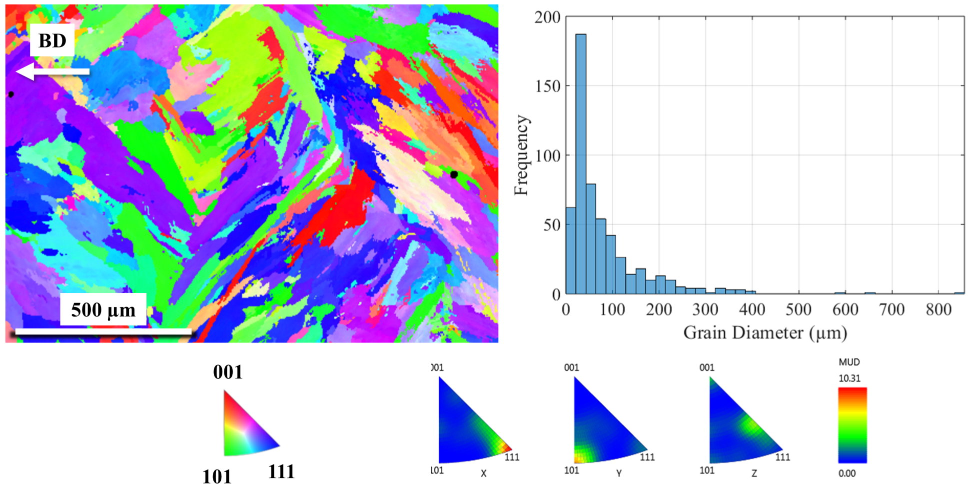

Fig. 2 Single alloy DED Inconel 625 IPFZ map, grain size distribution, and pole figures. The build direction is identified with an arrow on the IPF map.

images reveal an observable increase in porosity in the 50/50 layer when compared to the direct transition sample. Comparing the IPF maps of the two samples in **Figure 3** (c) and (d), in the direct transition sample, the stainless steel grains exhibit limited growth, without extending into the neighboring IN625 layers. This restriction can be attributed to the sudden change in material composition, leading to a lack of favorable conditions for the continued growth of the stainless steel grains. As a result, the stainless steel grains in the direct transition sample remain confined within their original boundaries. Conversely, in the 50/50 intermediate layers of the blended transition sample, the stainless steel grains demonstrate the ability to continue their growth. The stainless steel grains successfully extend their boundaries into the blended region. This phenomenon can be attributed to the gradual change in composition, allowing for an interfacial continuity that promotes grain growth. Overall, this comparison highlights the contrasting growth behaviors of stainless steel grains in the direct transition sample and the 50/50 SS316L-IN625 blend. While the direct transition restricts the growth of stainless steel grains, the blended sample enables their expansion into the intermediate layers, demonstrating the importance of material compatibility in facilitating grain growth with less discontinuities. Qualitatively, the grain morphology in the SS316L side of the 50/50 appears to be more equiaxed near the transition while the direct transition sample has SS316L grains that are more columnar. This is likely due to differences in the DED processing parameters or due to the addition of 50% SS316L in the intermediate layer of the 50/50 sample causing thermal properties to differ, and leading to columnar solidification.

Another noteworthy observation at the transition zone is pertaining to the distribution of elements in the final part. **Figure 4** represents the EDS results for the detected elements. Examining the interface in the Fe map, a low amount of Fe is seen to diffuse into the IN625 zone. **Figure 5** shows the EDS maps for the 50/50 sample where a larger area that spans the 50/50 blended zone (about 600 µm wide region) exhibits an Fe-rich area that is expected from the mixing of the SS316L powders and the IN625 powders during DED. Moreover, Fe-rich pocket-like zones are clearly identified near the transition line in **Figure 5** . It is postulated that the Fe-rich pockets are a result of elemental segregation during the deposition and solidification processes.

To further understand the behavior of the bimaterials, the micro-hardness of both transition strategies of the bimetallic specimens are measured and shown in **Figure 6**. For that purpose, a separate analysis specimen was fabricated by depositing IN625 on one end of a LPBF SS316L part in the direct transition and then depositing a 50/50 transition on the other end of the LPBF SS316L part. The micro-hardness of each single material and transition zone were tested. The pure IN625 exhibits HV values ranging between 241.5 and 277.1. The pure SS316L exhibits HV values ranging between 230.6 and 262.9. The direct transition strategy exhibits an average of 262.3 HV and the 50/50 transition a much lower average value of 232 HV. The authors hypothesize this is due to larger grains in the 50/50 region, or solid solution softening. It is observed that while the 50/50 transition was lower in hardness than both single

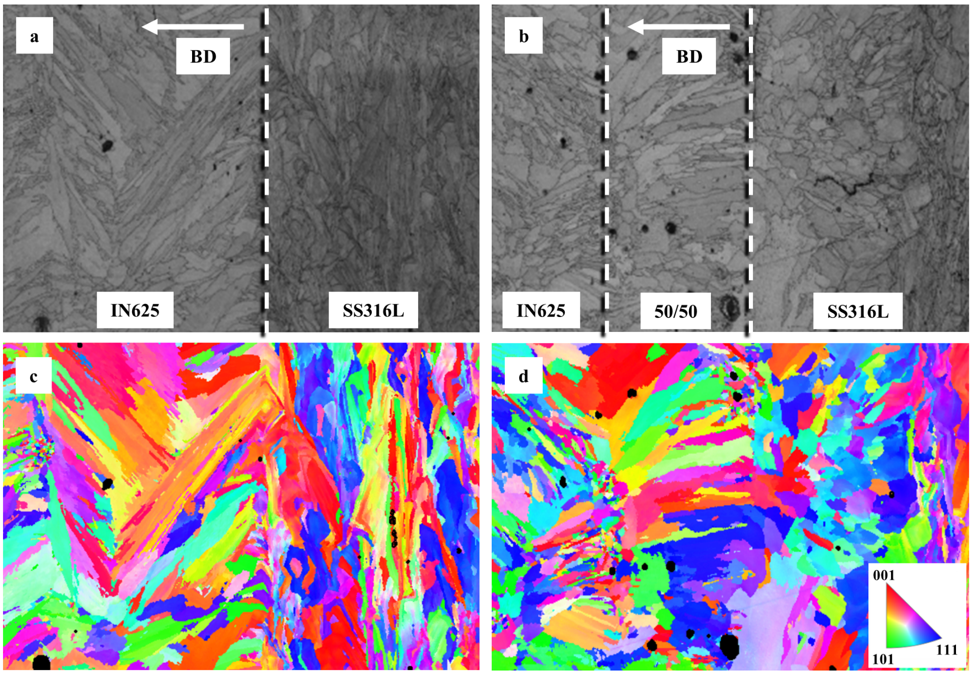

Fig. 3 Microstructural characterization of the bimetallic specimens fabricated using LPBF SS316L bases where IN625 is deposited. Two transition strategies are employed, namely a direct transition (a, c) and a 50/50 transition where an equal mix of the two powders is used over an equivalent of two DED layers (b, d). The transition zones are identified with a dashed line and further labeled on the figures. Figures (a-b) show the band contrast highlighting the grain boundaries, (c-d) show the IPF-Z maps revealing the grain orientations.

alloys, the Direct Transition had increased hardness comparable with the upper value in IN625. Therefore, it is recommended that for increased hardness when producing a bimetallic to use a direct transition rather than 50/50 when DED is used to deposit IN625 onto LPBF SS316L, or a thorough investigation into optimal properties of printing a 50/50 transition layer.

4 Conclusion

The microstructures of single alloy LPBF SS316L and DED IN625 were analyzed along with the combinatory alloys fabricated with a direct transition and a 50/50 mixed intermediate region. The 50/50 transition zone showed an increase in porosity

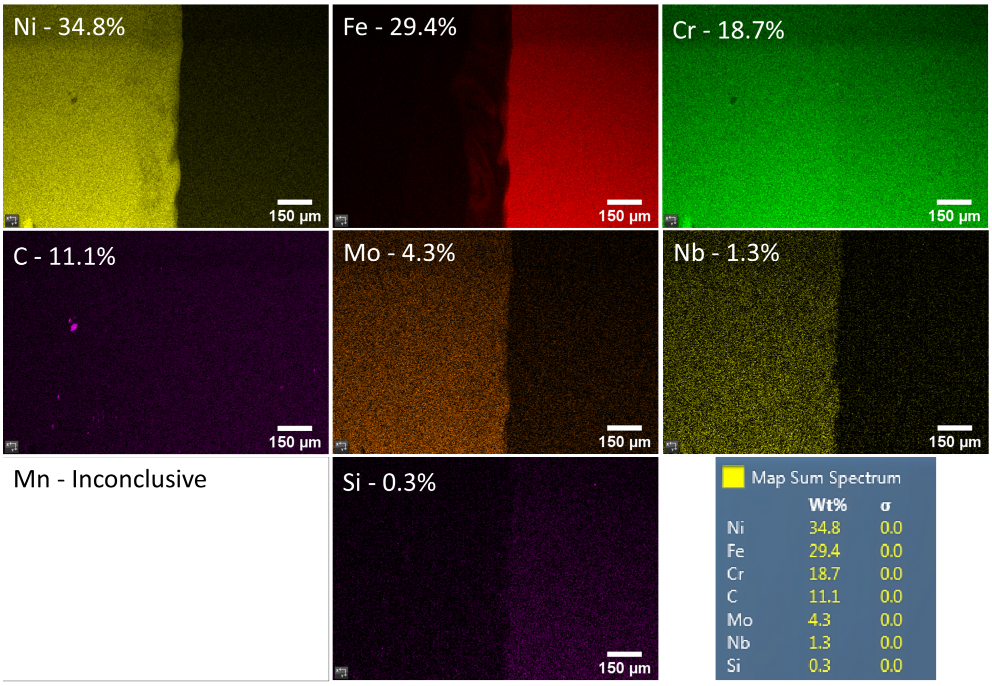

Fig. 4 EDS maps of the Direct Transition specimen showing elemental composition and the sum spectrum weight percentages.

when compared to the direct transition. Iron-rich zones in the 50/50 section imply elemental segregation during deposition and solidification of the DED mixed layers. Microhardness showed an increased hardness at the direct transition compared to the 50/50 transition. It is therefore recommended to ensure optimal properties are determined for a 50/50 transition when joining IN625 with LPBF SS316L using DED.

Future work directions to support the energy sector in adopting AM processes include a more comprehensive study on the development of parameters to fabricate the joint of the bimetallic samples. More EBSD scans would increase the sample size and validate trends shown in this work. Furthermore, the quality of the two transition strategies should be further investigated. Finally, by understanding the microstructure of the direct and 50/50 transition, industry and academia can design accordingly

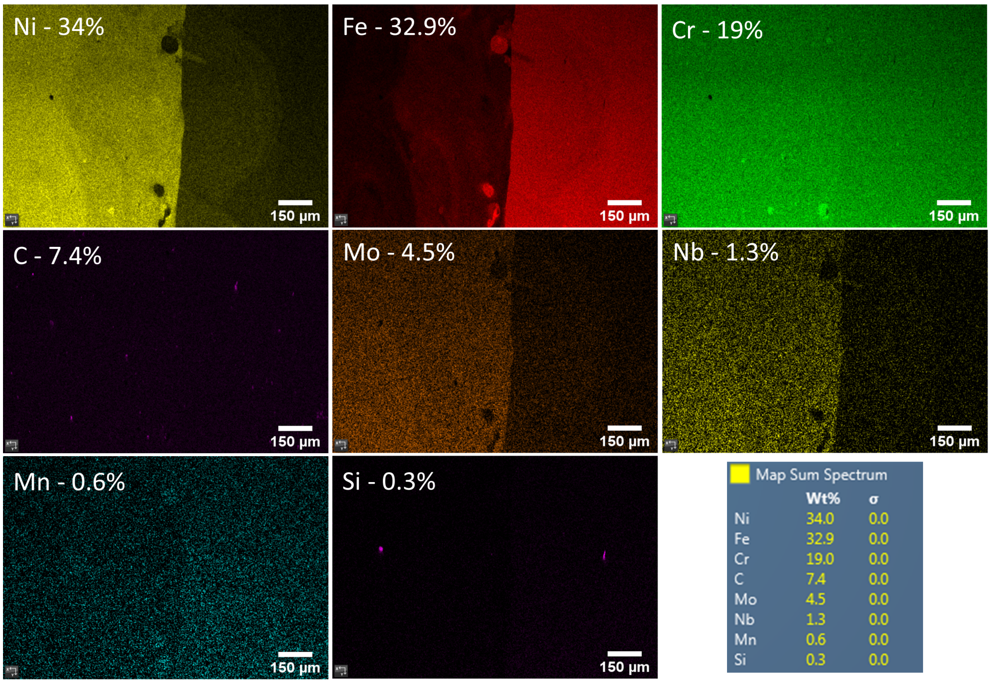

Fig. 5 EDS maps of the 50/50 Transition sample showing elemental composition and the sum spectrum weight percentages.

to make use of bimetallics fabricated by DED combined with LPBF to achieve cost savings and a reduced envelope for heat exchangers in the energy sector.

Acknowledgments. This material is based upon work supported by the U.S. Department of Energy, Office of Science, Office of Energy and Renewable Energy, Solar Energy Technologies Office (SETO) under Award Number DE-EE0009381. The authors acknowledge startup funding from Utah State University. The authors are grateful for the support from the Microscopy Core Facility at Utah State University for SEM characterization, and Formalloy for micro-hardness testing.

Declarations

On behalf of all authors, the corresponding author states that there is no conflict of interest.

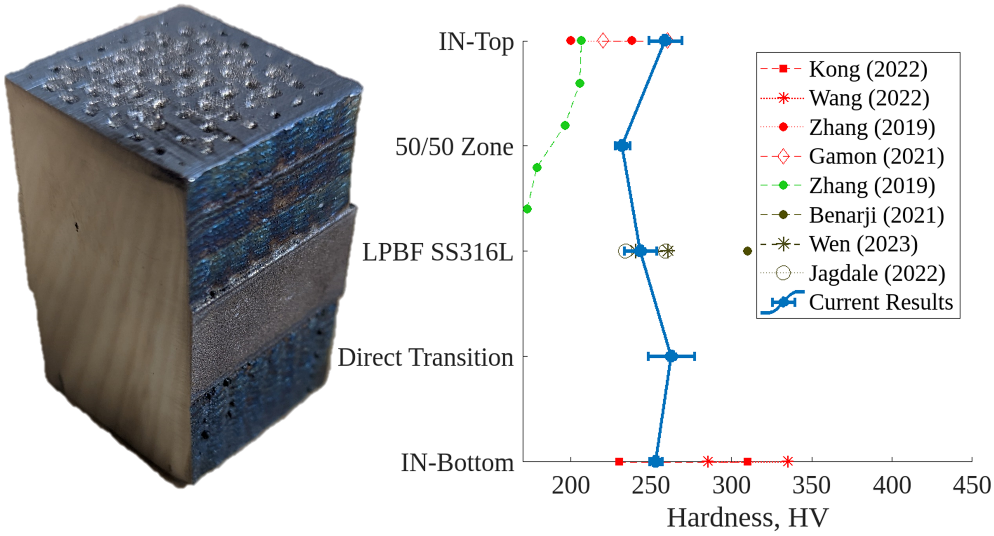

Fig. 6 **Left:** Image of the specimen fabricated by depositing IN625 DED onto the top and bottom of LPBF SS316L in a 50/50 transition (top portion) and direct transition (bottom portion). **Right:** Variability of the Vickers Hardness along each of the areas of interest including the single material and transition zones, and values from literature [33–39].

Appendix

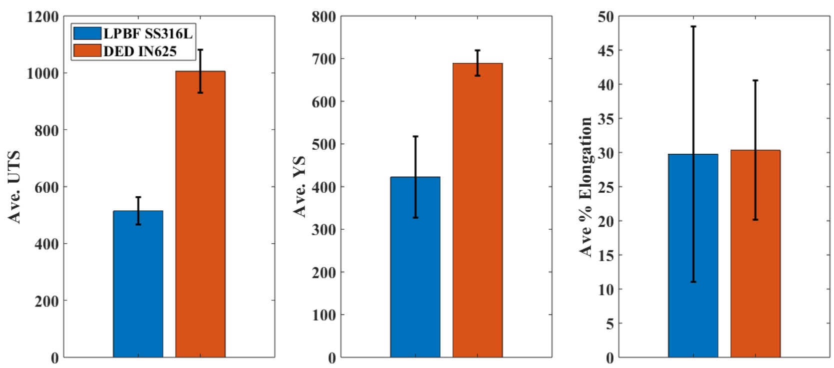

Fig. 7 Mechanical properties from literature for both SS316L processed by LPBF and IN625 fabricated via DED. Left: Average Ultimate Tensile Strength, Middle: Average Yield Strength, Right: Average Percent Elongation. [34, 40–43]

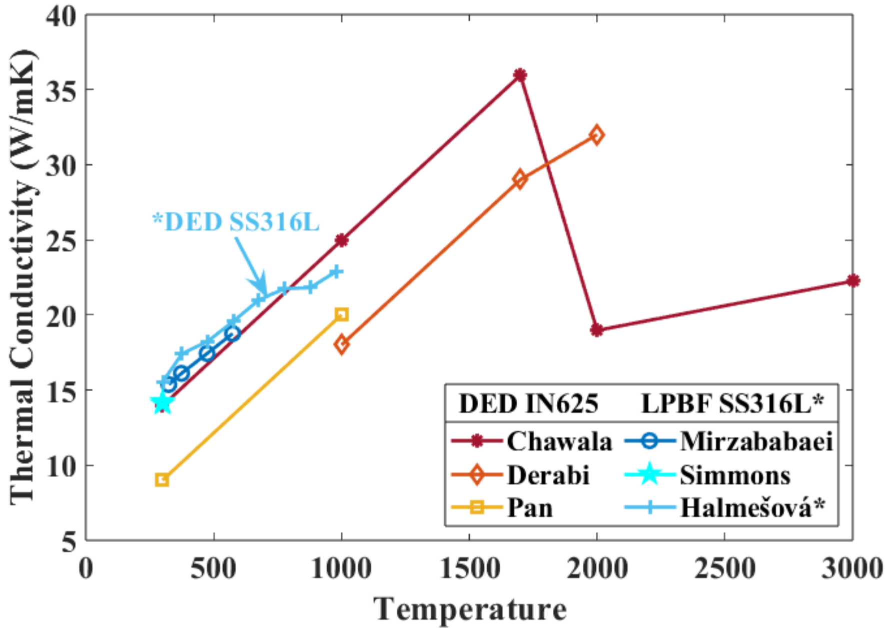

Fig. 8 Thermal conductivity values from literature for both DED IN625 (shown in red, yellow, and orange) and LPBF SS316L (shown in blue), with the exception of Halmesova et al. showing values for DED SS316L (indicated by arrow and asterisk.[43–48]

References

[1] Kerry, J., Mccarthy, G. y the United States Department of State and the United States Executive Office of the President, Washington DC (2021)

[2] Administration, E.I. Technical report, Energy Information Administration (March 2023). https://www.eia.gov/outlooks/aeo/narrative/index.php#ExecutiveSummary

[3] Administration, E.I. https://www.eia.gov/energyexplained/us-energy-facts/

[4] Zhang, H.L., Baeyens, J., Degrève, J., Cacères, G.: (2013). https://doi.org/10.1016/j.rser.2013.01.032 . https://linkinghub.elsevier.com/retrieve/pii/S1364032113000634

[5] Barlev, D., Vidu, R., Stroeve, P. Solar Energy Materials and Solar Cells **95**(10), 2703–2725 (2011) https://doi.org/10.1016/j.solmat.2011.05.020

[6] McDonald, C.F. Turbo Expo: Power for Land, Sea, and Air, vol. Volume 2: Coal, Biomass and Alternative Fuels; Combustion and Fuels; Oil and Gas Applications; Cycle Innovations, pp. 002–04018 (2000). https://doi.org/10.1115/2000-GT-0167 . https://doi.org/10.1115/2000-GT-0167

[7] McDonald, C.F. Applied Thermal Engineering **23**(12), 1463–1487 (2003) https://doi.org/10.1016/S1359-4311(03)00083-8

[8] Saleh, B., Jiang, J., Fathi, R., Al-hababi, T., Xu, Q., Wang, L., Song, D., Ma, A. Composites Part B: Engineering **201**, 108376 (2020) https://doi.org/10.1016/j.compositesb.2020.108376

[9] Wei, C., Zhang, Z., Cheng, D., Sun, Z., Zhu, M., Li, L. International Journal of Extreme Manufacturing **3**(1), 012003 (2020) https://doi.org/10.1088/2631-7990/abce04 . Publisher: IOP Publishing

[10] Dev Singh, D., Arjula, S., Raji Reddy, A. Materials Today: Proceedings **47**, 2450–2456 (2021) https://doi.org/10.1016/j.matpr.2021.04.536

[11] Schneck, M., Horn, M., Schmitt, M., Seidel, C., Schlick, G., Reinhart, G. Progress in Additive Manufacturing **6**(4), 881–894 (2021) https://doi.org/10.1007/s40964-021-00205-2

[12] Rasouli, E., Montgomery, C., Stevens, M., Rollett, A.D., Subedi, S., Mande, C.W., Narayanan, V.

[13] Tiwari, R., Andhare, R.S., Shooshtari, A., Ohadi, M. Applied Thermal Engineering **147**, 781–788 (2019) https://doi.org/10.1016/j.applthermaleng.2018.10.122

[14] Ding, M., Liu, J., Cheng, W.-L., Huang, W.-X., Liu, Q.-N., Yang, L., Liu, S.-Y. Applied Thermal Engineering **138**, 513–522 (2018) https://doi.org/10.1016/j.applthermaleng.2018.04.055

[15] Kaur, I., Singh, P. International Journal of Heat and Mass Transfer **178**, 121600 (2021) https://doi.org/10.1016/j.ijheatmasstransfer.2021.121600

[16] Wits, W.W., Amsterdam, E. CIRP Annals **70**(1), 159–162 (2021) https://doi.org/10.1016/j.cirp.2021.03.005

[17] Mussatto, A. Results in Engineering **16**, 100769 (2022) https://doi.org/10.1016/j.rineng.2022.100769

[18] Ali, S., Irfan, M., Niazi, U.M., Rani, A.M.A., Rashedi, A., Rahman, S., Khan, M.K.A., Alsaiari, M.A., Legutko, S., Petrů, J., Trefil, A. Materials **15**(8), 2822 (2022) https://doi.org/10.3390/ma15082822 . Number: 8 Publisher: Multidisciplinary Digital Publishing Institute

[19] Zhong, C., Kittel, J., Gasser, A., Schleifenbaum, J.H. Optics & Laser Technology **109**, 352–360 (2019) https://doi.org/10.1016/j.optlastec.2018.08.003

[20] Zhang, X., Chen, Y., Liou, F. Science and Technology of Welding and Joining **24**(5), 504–516 (2019) https://doi.org/10.1080/13621718.2019.1589086

[21] Su, Y., Chen, B., Tan, C., Song, X., Feng, J. Journal of Materials Processing Technology **283**, 116702 (2020) https://doi.org/10.1016/j.jmatprotec.2020.116702

[22] Hinojos, A., Mireles, J., Reichardt, A., Frigola, P., Hosemann, P., Murr, L.E., Wicker, R.B. Materials & Design **94**, 17–27 (2016) https://doi.org/10.1016/j.matdes.2016.01.041

[23] Chen, W.-Y., Zhang, X., Li, M., Xu, R., Zhao, C., Sun, T. Additive Manufacturing **36**, 101500 (2020) https://doi.org/10.1016/j.addma.2020.101500

[24] Singh, S.P., Aggarwal, A., Upadhyay, R.K., Kumar, A. Materials and Manufacturing Processes **36**(9), 1028–1039 (2021) https://doi.org/10.1080/10426914.2021.1885701 . Publisher: Taylor & Francis _eprint: https://doi.org/10.1080/10426914.2021.1885701

[25] Shah, K., Haq, I.u., Khan, A., Shah, S.A., Khan, M., Pinkerton, A.J. Materials & Design (1980-2015) **54**, 531–538 (2014) https://doi.org/10.1016/j.matdes.2013.08.079

[26] Wang, X., Muñiz-Lerma, J.A., Attarian Shandiz, M., Sanchez-Mata, O., Brochu, M. Materials Science and Engineering: A **766**, 138395 (2019) https://doi.org/10.1016/j.msea.2019.138395

[27] Sohrabpoor, H., Salarvand, V., Lupoi, R., Chu, Q., Li, W., Aldwell, B., Stanley, W., O'Halloran, S., Raghavendra, R., Choi, C.-H., Brabazon, D. Journal of Materials Research and Technology **12**, 210–220 (2021) https://doi.org/10.1016/j.jmrt.2021.02.090

[28] Jandaghi, M.R., Saboori, A., Iuliano, L., Pavese, M. Materials Science and Engineering: A **828**, 142109 (2021) https://doi.org/10.1016/j.msea.2021.142109

[29] Pratheesh Kumar, S., Elangovan, S., Mohanraj, R., Ramakrishna, J.R. Materials Today: Proceedings **46**, 7892–7906 (2021) https://doi.org/10.1016/j.matpr.2021.02.566

[30] Martin, N., Hor, A., Copin, E., Lours, P., Ratsifandrihana, L. Journal of Materials Processing Technology **303**, 117542 (2022) https://doi.org/10.1016/j.jmatprotec.2022.117542

[31] Hu, Y., Lin, X., Li, Y., Zhang, S., Zhang, Q., Chen, W., Li, W., Huang, W. Materials Science and Engineering: A **817**, 141309 (2021) https://doi.org/10.1016/j.msea.2021.141309

[32] Chen, F., Wang, Q., Zhang, C., Huang, Z., Jia, M., Shen, Q. Journal of Alloys and Compounds **917**, 165572 (2022) https://doi.org/10.1016/j.jallcom.2022.165572

[33] Kong, Y., Huang, H. Materials & Design **224**, 111279 (2022) https://doi.org/10.1016/j.matdes.2022.111279

[34] Wang, J., Wang, Y., Su, Y., Shi, J. Materials Science and Engineering: A **830**, 142296 (2022) https://doi.org/10.1016/j.msea.2021.142296

[35] Zhang, X., Chen, Y., Liou, F. Science and Technology of Welding and Joining **24**(5), 504–516 (2019) https://doi.org/10.1080/13621718.2019.1589086

[36] Gamon, A., Arrieta, E., Gradl, P.R., Katsarelis, C., Murr, L.E., Wicker, R.B., Medina, F. Results in Materials **12**, 100239 (2021) https://doi.org/10.1016/j.rinma.2021.100239

[37] Benarji, K., Ravi Kumar, Y., Jinoop, A.N., Paul, C.P., Bindra, K.S. Metals and Materials International **27**(3), 488–499 (2021) https://doi.org/10.1007/s12540-020-00838-y

[38] Wen, Y., Gao, J., Narayan, R.L., Wang, P., Zhang, L., Zhang, B., Ramamurty, U., Qu, X. Materials Science and Engineering: A **862**, 144515 (2023) https://doi.org/10.1016/j.msea.2022.144515

[39] Jagdale, S.H., Theeda, S., Ravichander, B.B., Kumar, G. (2022). https://doi.org/10.26153/tsw/44546 . Accepted: 2023-03-28T19:21:07Z. https://repositories.lib.utexas.edu/handle/2152/117667

[40] Gu, D., Chen, H. Materials Science and Engineering: A **725**, 419–427 (2018) https://doi.org/10.1016/j.msea.2018.04.046

[41] Lavery, N.P., Cherry, J., Mehmood, S., Davies, H., Girling, B., Sackett, E., Brown, S.G.R., Sienz, J. Materials Science and Engineering: A **693**, 186–213 (2017) https://doi.org/10.1016/j.msea.2017.03.100

[42] Karmuhilan, M., Kumanan, S. Journal of Materials Engineering and Performance **31**(4), 2583–2592 (2022) https://doi.org/10.1007/s11665-021-06427-3

[43] Pan, T., Zhang, X., Yamazaki, T., Sutton, A., Cui, W., Li, L., Liou, F. The International Journal of Advanced Manufacturing Technology **109**(5), 1261–1274 (2020) https://doi.org/10.1007/s00170-020-05713-z

[44] Chawla, T.C., Graff, D.L., Borg, R.C., Bordner, G.L., Weber, D.P., Miller, D. Nuclear Engineering and Design **67**(1), 57–74 (1981) https://doi.org/10.1016/0029-5493(81)90155-2

[45] Darabi, R., Ferreira, A., Azinpour, E., Sa, J.C., Reis, A. The International Journal of Advanced Manufacturing Technology **119**(5), 3975–3993 (2022) https://doi.org/10.1007/s00170-021-08376-6

[46] Mirzababaei, S., Doddapaneni, V.V.K., Lee, K., Paul, G.E., Pirgazi, H., Tan, K.-S., Ertorer, O., Chang, C.-h., Paul, B.K., Pasebani, S. Additive Manufacturing **70**, 103576 (2023) https://doi.org/10.1016/j.addma.2023.103576

[47] Simmons, J.C., Chen, X., Azizi, A., Daeumer, M.A., Zavalij, P.Y., Zhou, G., Schiffres, S.N. Additive Manufacturing **32**, 100996 (2020) https://doi.org/10.1016/j.addma.2019.100996

[48] Halmešová, K., Trojanová, Z., Koukolíková, M., Brázda, M., Džugan, J., Huang,

W. Journal of Alloys and Compounds **927**, 167082 (2022) https://doi.org/10.1016/j.jallcom.2022.167082